## NANOSTRUCTURES

# Electrochemical electron beam lithography: Write, read, and erase metallic nanocrystals on demand

Jeung Hun Park,[1,2,3] Daniel A. Steingart,[2]* Suneel Kodambaka,[1]* Frances M. Ross[3]*

We develop a solution-based nanoscale patterning technique for site-specific deposition and dissolution of metallic nanocrystals. Nanocrystals are grown at desired locations by electron beam–induced reduction of metal ions in solution, with the ions supplied by dissolution of a nearby electrode via an applied potential. The nanocrystals can be "erased" by choice of beam conditions and regrown repeatably. We demonstrate these processes via in situ transmission electron microscopy using Au as the model material and extend to other metals. We anticipate that this approach can be used to deposit multicomponent alloys and core-shell nanostructures with nanoscale spatial and compositional resolutions for a variety of possible applications.

## INTRODUCTION

Fabrication of site-specific nanostructures of desired shape, structure, and composition is probably the most desirable goal pursued actively by the nanotechnology community (1). In particular, metallic nanostructures have a wide variety of applications that include biosensors, photonics, and energy storage/conversion devices (2). To fabricate aperiodic, nanoscale metallic patterns on arbitrary substrates, top-down nanofabrication technologies have been developed (3). Photon and electron beam lithographies generally require the use of photoresist and involve vacuum deposition (4). In contrast, resist-free approaches and potentially simpler pathways to fabricate metallic nanostructures in a single process step (5, 6) are attractive. Resist-free direct writing approaches include focused ion beam–assisted (5) and electron beam–assisted (6) deposition of metallic nanostructures and dip-pen nanolithography (7). These approaches enable one-step nanoscale fabrication with in situ metrology (7) and imaging (8). Complementary to these techniques, the ability to deposit materials via solution medium can potentially allow a wider choice of materials and is beneficial for direct deposition of complex nanoscale three-dimensional patterns (9). Solution-phase versions of electron beam– or ion beam–induced deposition have therefore been developed to fabricate various metallic and semiconducting nanostructures and thin films (7, 9). However, these beam-driven processes have significant limitations (9). For example, metalorganic precursors typically yield metal grains embedded in an amorphous matrix (10). Fluoro- and chlorophosphine-based precursors cause significant phosphorus incorporation into Au, Pt, Ni, and Co deposits and are also toxic, unstable, and expensive (11, 12). The flexibility required to deposit arbitrary alloys and multiple materials is limited (9, 10) because the existing methodologies require the metals to be present in the precursor, which must therefore be optimized for the particular element or alloy of interest. Electrochemical techniques can produce patterned metallic deposits, but the substrate must be conductive: For example, laser-induced plating (13) uses thermal effects to increase the electrochemical deposition rate over areas of tens of micrometers in size, and electron beam–induced plating (14) forms patterns with length scales of tens of nanometers.

Here, we report the development of a solution-based technique for site-specific nanoparticle deposition that supplies the material of interest via electrochemical control, but uses an electron beam to define the location at which this material is deposited in the form of nanoclusters. Both electrochemical and irradiation parameters influence growth, and the deposit can be "erased" by a suitable choice of irradiation conditions. The multitude of control factors suggests that few-nanometer precision may be achievable in the dimensions of the nanostructures produced. We apply this technique to deposit several different metals. In principle, simultaneous deposition of multiple materials to form alloys, or sequential deposition to form compositionally modulated core-shell structures, can be achieved through inclusion of a separate "source" for each material. This provides a potentially useful flexibility compared to existing beam-induced deposition techniques. Analogous to the existing approaches for electron beam–induced patterning, control of deposit position should be achievable via the beam irradiation parameters.

## RESULTS

As a proof of concept, we demonstrate this lithography technique using in situ liquid cell transmission electron microscopy (TEM). In the TEM liquid cell (see the Supplementary Materials), a thin layer of liquid, below a few hundred nanometers in thickness, fills the space between two electron-transparent windows, each a 50-nm-thick silicon nitride film. For the experiments described below, several metal thin-film electrodes are patterned on the interior surface of one window of the liquid cell. The electrode areas are of the order of 100 $\mu m^2$, and the separation between electrodes is several tens of micrometers. In each experiment, all electrodes are composed of the same metal (Au, Ni, or Cu). The liquid cell is filled with an electrolyte, generally 0.1 M HCl (pH 1). A pair of electrodes is used for each experiment. To form the metal nanocrystals, a potential is applied across the electrodes, and the electron beam is located between the electrodes and focused to a diameter of several micrometers. We have examined potentiostatic conditions, in which a fixed potential of typically a few hundred millivolts is applied between the electrodes, and galvanostatic conditions, in which a current typically a few tens of nanoamperes is flowed between the electrodes. In both cases, a pulsed mode is used in which potential or current is switched periodically on and off (see, for example, fig. S1). The spread beam and pulsed mode facilitate investigation of the deposition kinetics, and pulsing also avoids electrochemically generated gas bubbles at the electrodes (15) because bubbles cause

[1]Department of Materials Science and Engineering, University of California, Los Angeles, 410 Westwood Plaza, Los Angeles, CA 90095, USA. [2]Department of Mechanical and Aerospace Engineering, and Andlinger Center for Energy and the Environment, Princeton University, Princeton, NJ 08544, USA. [3]IBM Thomas J. Watson Research Center, 1101 Kitchawan Road, Yorktown Heights, NY 10598, USA.
*Corresponding author. Email: steingart@princeton.edu (D.A.S.); kodambaka@ucla.edu (S.K.); fmross@us.ibm.com (F.M.R.)

difficulties in interpreting liquid cell TEM data (16). As the electrochemical cycling takes place, the growth of nanostructures in the illuminated area is recorded at 30 images/s. After the potential is switched off, a larger area can be imaged to measure any growth outside the illuminated region.

In this arrangement, metal ions are supplied electrochemically by an oxidation reaction, such as dissolution of Au at the counter electrode (CE), when an appropriate potential is applied. The released ions diffuse outward from the electrode. Some are deposited in the reduction reaction at the working electrode (WE), but any ions that diffuse to the irradiated area are reduced to zero-valent metal by reactive species produced when the electron beam irradiates the electrolyte. This phenomenon of metal deposition has been noted in liquid cell experiments involving biasing (17).

We first show the outcome of this process and then discuss its two key stages in more detail below. Figure 1A shows Au nanocrystals formed in the irradiated region of an HCl electrolyte when pulsed galvanostatic conditions are applied to Au electrodes. The corresponding movie and additional images are shown in movie S1 and fig. S1A, respectively. The nanocrystal morphology is three-dimensional, polycrystalline spiky balls, similar to the structures that have been grown elsewhere via chemical reduction processes in liquid precursors containing Au ions (18). Measurements of the radius of each nanocrystal show that growth is correlated with the electrochemical stimulus (Fig. 1B). As each current pulse occurs, growth takes place in a burst with measured radial growth rates as high as 20 to 50 nm s$^{-1}$. The onset of growth is similar for all the nanocrystals within the field of view. However, current alone does not predict growth because no growth was observed in the first four current cycles of this experiment (fig. S1). Instead, growth occurs only during the times at which the potential has become more negative than a threshold value, $V_{th}$ = −0.73 V in Fig. 1. This threshold is consistent, with a variation of less than 50 mV in the potential required for visible growth. With zero current or potential, the electrolyte can be irradiated for long periods of time (tens of minutes) without nanocrystal formation.

To clarify the source of the Au ions, we show the microstructural changes taking place at the CE as the potential is slowly varied through a critical value of −0.7 V in Fig. 2 and movie S2. Dissolution of the Au electrode is visible when the potential reaches −0.66 ± 0.03 V. The Au film thins and forms pits, followed by perforations (fifth and subsequent images in Fig. 2). This electrochemical corrosion process is related to electrorefining (19) and requires a specific onset (stripping) potential (20, 21); the measured value is consistent with the stripping (or sedimentation) potential for Au in acidic solutions (table S1). The similar potentials required for dissolution of the CE and visible nanocrystal growth in Fig. 1 provide strong evidence that the nanocrystals grow from Au ions released from the CE. Furthermore, analysis of Fig. 2B (see caption) shows that dissolution can supply enough ions to feed the observed growth rates (Fig. 2 shows a dissolution rate of 0.2 nm/s or $2 \times 10^{10}$ Au ions/s; Fig. 1 shows a radiolytic growth rate of $\sim 4 \times 10^9$ Au/s).

Under conditions when current rather than potential is controlled, as in Fig. 1, the delay in nanocrystal nucleation can be understood through the sequence of electrochemical reactions that take place at the CE. When current first flows, we expect electrolysis of the dilute HCl electrolyte to proceed through reduction of H$^+$ ions to H$_2$ at the WE and oxidation of Cl$^-$ at the CE. (Both gases are somewhat soluble in water, although we do observe gas bubbles if current is flowed for longer periods.) However, Cl$^-$ ions are likely to be rapidly depleted
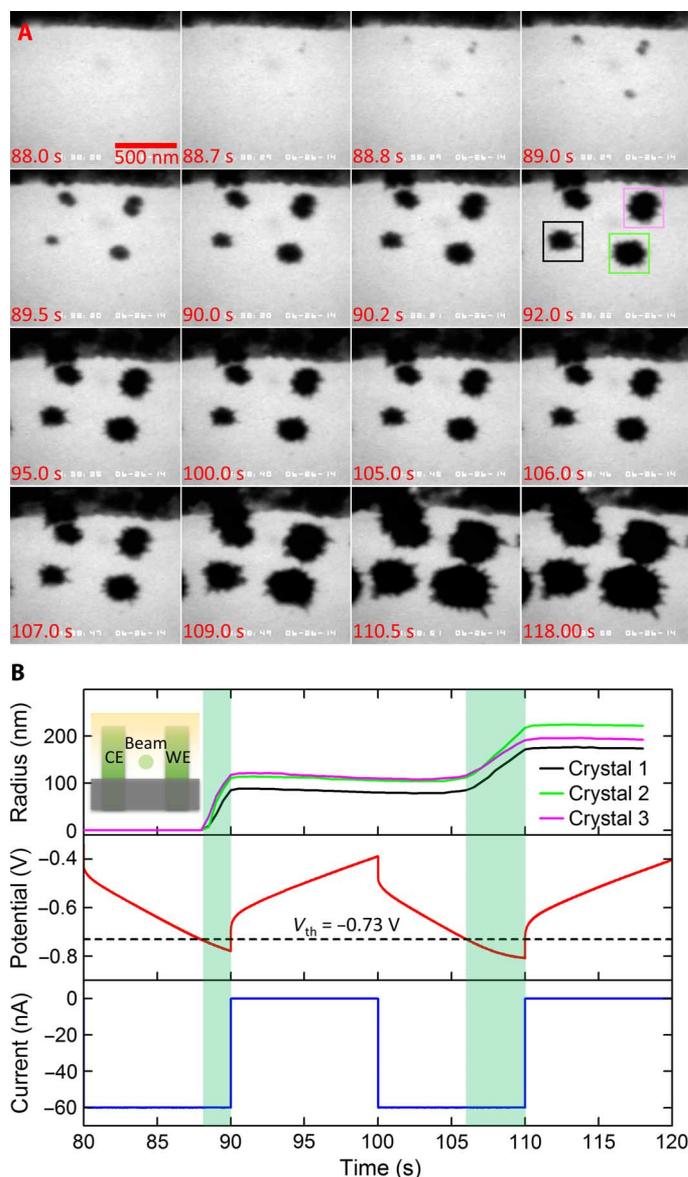


**Fig. 1. Electron beam–induced deposition process of Au nanocrystals under electrochemical control. (A)** Time sequence of bright-field TEM images obtained in a liquid cell showing the size evolution of one Au nanocrystal (among seven growing within the field of view) during pulsed galvanostatic electrochemical deposition in 0.1 M HCl. The electron dose rate is 46 $e^-$/Å$^2$·s. The full sequence is shown in movie S1, and additional images of the whole irradiated area are shown in fig. S1A. **(B)** Driving current (−60 nA in 10-s pulses), the resulting measured potential, and the radius versus time of three of the nanocrystals. The black, green, and magenta boxes shown in (A) at 92 s correspond to crystals 1, 2, and 3 in (B), respectively. Growth did not occur during the first four current pulses, only starting when the potential went below a threshold value $V_{th}$ ~ −0.73 V. Note that when the current is off, the radii decrease slightly under the beam. Light green shading indicates times at which nanocrystal growth was observed, consistently at potentials below −0.70 V. The smallest observable nanocrystal is around 25 nm in diameter (second image).

from the regions around the electrodes because of the small volume of electrolyte available in the liquid cell, even with the pauses in the current flow. The electrode potential therefore gradually becomes more negative over several cycles (Fig. 1B and fig. S1B) until it supports other reactions that can provide the set current. Oxidation of OH$^-$
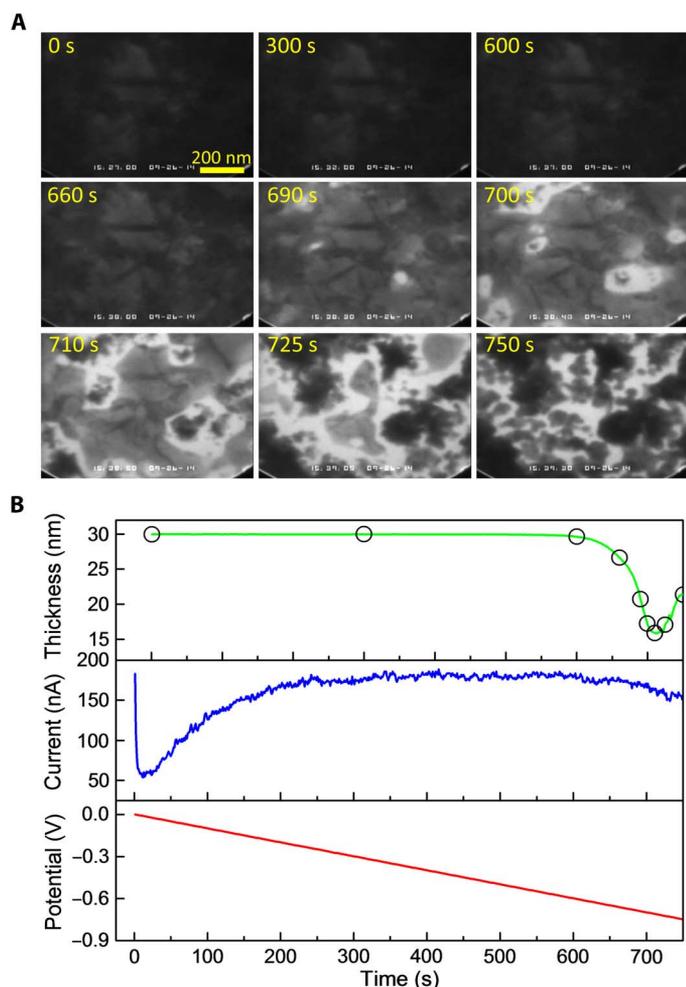
**Fig. 2. Electrochemical control of Au ion supply via the oxidation and dissolution of the Au CE.** (**A**) Microstructural evolution of the Au CE during linear sweeping potentiometry. A series of bright-field TEM images was recorded near the center of a 30-nm-thick Au electrode in 0.1 M HCl as the potential was swept from 0 to 0.75 V at 1 mV/s. The beam conditions were constant at a dose rate of 46 $e^-$/Å²·s. The complete data set is shown in movie S2. (**B**) Applied potential, measured current, and remaining thickness of Au (estimated from the transmitted brightness) are plotted as a function of time. If measured over the interval between −0.66 and −0.73 V, this thickness change corresponds to the release of $2 \times 10^{10}$ Au ions/s over the area of the electrode. The times of the images in (A) are indicated with open circles (○). The apparent increase in thickness after 710 s is caused by electron beam–induced redeposition of Au in areas where the electrode has been removed. All images were obtained with the same field of view.

can take place as the overpotential rises, but the concentration of OH⁻ is low, so it is not surprising that oxidation of Au occurs eventually from the CE. We expect oxidation and dissolution of the Au CE to be initiated concurrently in acid electrolytes (20, 21).

Controlling the potential provides a reasonably precise way to regulate nanocrystal growth. In fig. S2A and movie S3, we monitor growth as the potential is changed in 50-mV steps to confirm directly that growth initiates and continues while the potential is below −0.7 V. In fig. S2B and movie S4, we use the $V_{th}$ values derived in Figs. 1 and 4A to switch growth on and off by switching the potential between two values above and below the threshold value. A final example of nanocrystal control via potential is presented in fig. S4, which shows the effect of different electrochemical parameters on particle size and

morphology by comparing growths with different current on/off profiles. For identical charge passed, the number and size of nanocrystals increase when the current is applied over fewer but longer intervals (fig. S4A); in a single pulse, the amount of deposited material is not proportional to pulse length. This is because the potential exceeds $V_{th}$ for only a subset of the pulse time. No growth is expected for short pulses because the voltage does not reach the point at which Au ions are generated. If we assume that once the voltage exceeds $V_{th}$ all current is supplied by dissolution of the CE, then we expect the relationship between ions emitted and pulse length to be approximately linear with an offset of ~1 s (fig. S4B).

We now discuss the conversion of the released ions into nanocrystals. The formation of metal nanocrystals from metal ions in an irradiated solution is well established (22, 23). Irradiation of water by any high-energy x-rays, electrons, or γ-rays deposits energy into the water, breaking chemical bonds and creating molecular and radical products (24, 25). Key products include $e_h^-$ (hydrated or solvated electrons), H·, OH·, $H_2$, $H_2O_2$, and $H_3O^+$. Calculations that account for the formation rate of each product, its destruction due to reactions with other species, and its diffusion out of the irradiated area show that within milliseconds, for typical TEM liquid cell conditions, each radiolysis product reaches a steady-state concentration, which depends on dose rate and position (24, 25). Some radiolysis products can diffuse far from the irradiated area, but $e_h^-$, in particular, is so reactive that its concentration is high only where it is generated within the irradiated area and for a few nanometers outside (23–25).

Metal ions in solution react with one or more of the radiolytic species, most importantly $e_h^-$. For example, $Au^{3+}$ is reduced via a sequence of reactions that result in $Au^0$ (23), ultimately depositing Au in the form of nanocrystals. Liquid cell TEM experiments have visualized nanocrystal growth in solutions containing Au as well as Ag, Pd, Pt, and other ions (26 and references therein). Growth is confined to the irradiated area, given the minimal outward diffusion of $e_h^-$ discussed above. Nanocrystals may nucleate in the bulk of the solution or on the interior surfaces of the windows (27, 28). Depending on the conditions, nanocrystal growth rates may be determined either by the electron dose rate (production rate of $e_h^-$) or by the rate of supply of the metal ions from the unirradiated bulk solution (22, 23, 25). In the present experiments, where growth occurs only when ions are released from the electrode, the growth rate is clearly limited by the arrival of metal ions at the irradiated area, where they react with $e_h^-$ created by the beam.

The process shown in Fig. 1 differs from previous examples of beam-induced nanocrystal growth because metal ions are not initially present in solution. Instead, the electrochemical supply route of the ions enables "on-demand writing" via electrochemical control even under steady irradiation conditions. The geometry of the ion diffusion outward from the CE is visible in several of the images in Fig. 3, where deposition is greater around the periphery of the irradiated volume and in the direction of the CE.

We can estimate whether electrochemically released Au ions reach concentrations that can lead to radiolytic growth using simplifying assumptions. Solving the diffusion equation with flux boundary condition corresponding to the current and electrode geometry (fig. S5A) shows that the ion concentration a few micrometers from the source can reach 0.1 M, above the values used for beam-induced growth experiments, in a few tenths of a second. We further note that if the beam is placed far from the CE, we do not observe nanocrystal formation. Far from the electrode, the concentration does not reach
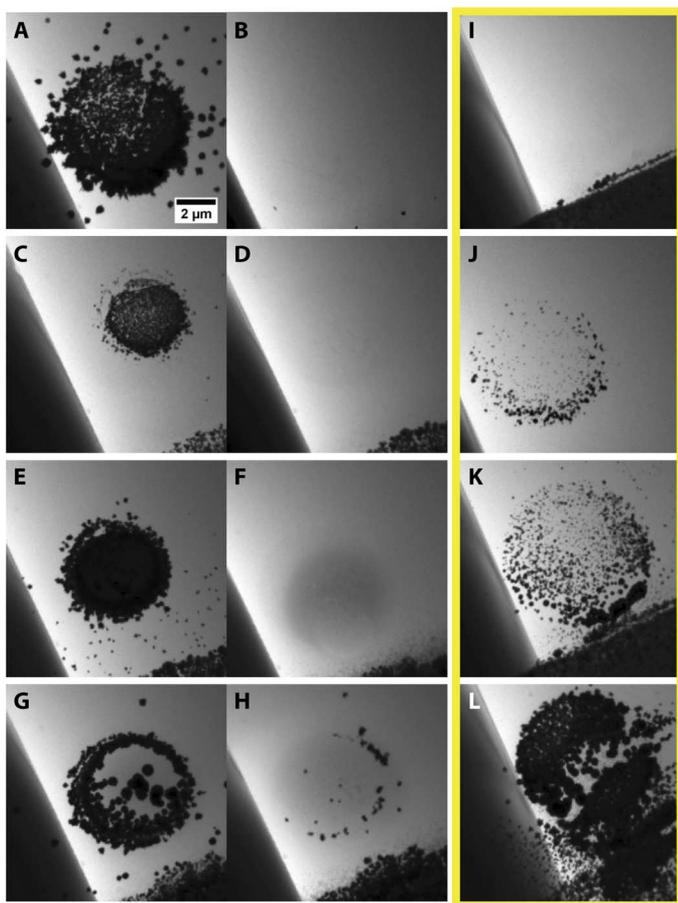
**Fig. 3. Series of bright-field liquid cell TEM images showing sequential writing and erasing of Au nanocrystals.** The images were obtained after writing or erasing was complete, spreading the beam to image an area larger than the area irradiated during the experiment. (**A** to **H**) Image pairs showing writing (A, C, E, and G) at a dose rate 46 $e^-/\text{Å}^2\cdot$s and a current or potential described below, followed by etching (B, D, F, and H) at a higher dose rate, $d_c \sim 260$ $e^-/\text{Å}^2\cdot$s, and zero applied potential. (A) First writing: Nanocrystals formed after 14 deposition cycles, each consisting of 5 s at −60 nA and 5 s at 0 nA. (B) Erasing of the first deposits at 0 nA. (C) Second writing: Nanocrystals formed after seven deposition cycles, each consisting of 5 s at −60 nA and 5 s at 0 nA. (D) Erasing of the second deposits at 0 nA. (E) Third writing using the stepped potential shown in fig. S2A, scanning from −0.3 to −0.8 V with 10-s 0.05-V steps. (F) Erasing of third deposits at 0 V. (G) Fourth writing using the potential shown in fig. S2B, −0.75 V for 10 s followed by −0.65 V for 10 s. (H) Erasing of the fourth deposits at 0 V. (**I** to **L**) Morphologies obtained using different modulations of a −60-nA current. Current was applied for 2 s (I), 3 s (J), 4 s (K), and 6 s (L) at −60 nA, respectively, followed by 2 s at 0 nA. Circular shadows in (F) and (H) are due to radiation damage of the silicon nitride windows during the long experiment. Additional images from the sequences are shown in figs. S3 and S4. All images were obtained with the same field of view.

the levels required for nucleation during the experiment. We do not expect an effect of electric field on diffusion of Au ions (or $e_h^-$) due to screening because the Debye length in the 0.1 M HCl electrolyte is only a few nanometers.

The ability to optimize both electrochemical and irradiation parameters provides opportunities for control of nanocrystal growth by subtraction as well as addition. Dissolution is possible because although $e_h^-$ is a strong reducer, other radiolytically produced species

such as OH⁻ are oxidizers. The steady-state balance of radiolysis species depends on the dose rate, with simple calculations suggesting that higher dose rates should result in a higher ratio of oxidizing to reducing species (25). Dissolution processes are therefore expected to be stronger at high dose rates. Competitive oxidation and reduction reactions have been observed in liquid cell experiments depending on dose rate (25, 29). At high enough dose rates, previously formed nanocrystals can be removed. Figure 3A and fig. S3 demonstrate a sequential process of growth (writing) and radiolytic dissolution (erasing) of Au nanocrystals. Particles are "written" under a moderate dose rate with an appropriate potential. Growth stops as soon as the potential is set to zero because rapid diffusion lowers the concentration of ions (fig. S5B). Particles are erased by then increasing the dose rate, either by focusing the beam and scanning it slowly over the existing nanocrystals or by increasing the emission current at constant beam size. Writing and erasing can be repeated multiple times. In this experiment, the ensemble of nanocrystals grew at ~2 × 10¹⁰ Au ions/s at a dose rate of ~5 × 10³ $e^-/\text{nm}^2\cdot$s and a potential of −0.7 V. They were virtually unchanged after many (tens of) hours at this dose rate with 0 V, but increasing the dose rate to 2.6 × 10⁴ $e^-/\text{nm}^2\cdot$s (at 0 V) caused etching at ~5 × 10⁸ Au ions/s. Etch rates are generally slower than growth rates under the conditions accessible in the experiments. Size control of nanocrystals may thus be optimized by first growing and then tuning the size by etching. Figure S6 and movies S5 and S6 illustrate this via writing and erasing an ensemble of small crystals.

To address the generality of this technique, we have tested other metal electrodes, Ni and Cu, with the same electrolyte (Fig. 4, fig. S7, and movies S7 and S8), and Au with other electrolytes. Dissolution and deposition processes appear similar for Cu, Ni, and Au. The measured potentials for nanocrystal formation are summarized in table S1. Different potentials are required for each metal, with the onset potential related to the literature stripping potentials but also depending, to some extent, on the geometry of the electrodes due to our two-terminal (pseudo–reference electrode) configuration. In addition to 0.1 M HCl, we tested 0.1 M ZnCl₂ (pH 2.5). This solution is stable to beam irradiation for over 2 hours at 3 × 10⁴ $e^-/\text{nm}^2\cdot$s. We find that Au nanocrystal formation requires a potential of −0.7 V, similar to that required in 0.1 M HCl. However, at a fixed potential above this value, the growth rate of Au nanocrystals in ZnCl₂ is slower than in HCl; the time taken for complete dissolution of the Au CE in ZnCl₂ is also slower than in HCl (~30 and 4 min, respectively, on pulsing the current at −60 nA for 10 s with 10 s off times). Because the dissolution process at the CE scales linearly with H⁺ concentration (21), we would expect a higher dissolution rate of Au in HCl and hence a higher supply rate of Au ions to the irradiated area.

## DISCUSSION
The methodology that we have described for liquid-phase synthesis of nanocrystals involving electrochemical and radiolytic control parameters is summarized in fig. S8. The growth and etching kinetics of nanocrystals are controlled both via selective electrochemical dissolution, which determines the supply of metal ions, and electron beam irradiation, which determines the growth location and can determine the size. Because the metal ions do not need to be supplied in the liquid phase, the method is flexible in the choice of metals and substrate. It may be possible to include multiple metal electrodes that can be selectively and sequentially activated to create more complex structures, such as core-shell or alloy nanocrystals. We can also envisage

**Fig. 4. Electrochemical + radiolytic formation of Au, Cu, and Ni nanocrystals.** All growths occur in 0.1 M HCl during linear potential sweeping at 1 mV/s for Au, 5 mV/s for Cu, and 1 mV/s for Ni. The measured onset potentials are shown in table S1 and other electrochemical parameters are shown in fig. S7. All images are obtained at the same field of view.

designing the geometry of the electrodes to supply material from different directions, possibly enabling fabrication of asymmetrical structures such as Janus particles. This flexibility in materials supply is an advantage compared to other electron beam–induced deposition techniques, where the solution typically contains micromolar to millimolar concentrations of ionic complexes and must be tuned for each alloy.

We expect the location of a nanocrystal to be controllable by choosing a small spot size and exploiting the limited presence of the radiolysis species outside the beam. A nanometer-scale liquid interaction volume is possible, in principle, using small probe sizes in scanning TEM (STEM) (30). The minimum size of the deposit is similarly expected to be strongly dependent on the beam size and energy as well as on the ion supply. The smallest feature sizes demonstrated in optimized lithography tools for electron beam–induced deposition in liquids are in the 20- to 30-nm range (31); in STEM, feature sizes down to 40 nm have been demonstrated (32). The crystal size is controllable because the total number of ions can be specified, as shown in Fig. 1, unlike conventional beam–induced patterning where the reservoir is effectively infinite. Furthermore, particle etching (and, although not demonstrated, pulsing of the beam) are additional controls in our method that may help to achieve smaller-dimension deposits. State-of-the-art STEM with nanoscale beam sizes may thus allow deposition of materials with few-nanometer dimensions, similar to what has been demonstrated in gas-phase beam-induced deposition (33, 34). This degree of control will require calibration. Fortunately, imaging without growth is straightforward once the voltage is off, and a feedback approach to monitoring the size of beam-induced particles may be relevant (32).

Because other energetic radiation can reduce metal ions, focused laser light may also form analogous structures, although at larger dimensions. The solution composition provides additional parameters for tuning particle growth kinetics and morphology. Solution composition, including pH, affects the stability of dissolved ions and nanocrystals (23); particle shape should be tunable by introducing surfactants (35, 36). The introduction of scavenger species (37) can, in principle, optimize the concentrations and types of radiolysis products formed and can even modify the diffusivities of reacting species and change the balance of etching and growth (25). Solution composition will also affect the required potential (20, 21, 38). Finally, if particular elements present contamination problems [such as chlorine (32)], then it may be possible to choose an electrolyte that avoids them. Overall, the use of both dose rate and electrochemical control in the process described here provides a variety of parameters to tune the growth.

Finally, we note that accurate determination of the onset potential for a dissolution process can be difficult to achieve using conventional experimental techniques such as cyclic voltammetry (20). Visualiza-

tion of ions in solution via radiolytic deposition can therefore perhaps provide useful information in corrosion studies. It may also be possible to measure diffusion processes by using the electron beam as a probe of ion concentration as a function of time and space. This in situ growth scheme therefore offers new venues to synthesize complex nanostructures and quantify liquid-phase processes.

## MATERIALS AND METHODS
### Growth platform
The growth experiments were performed in an electrochemical liquid cell (Hummingbird Scientific) with flow capabilities, operated inside a 300-kV TEM (FEI CM30 TEM). The results reported here were obtained with the cell completely filled with electrolyte, without gas bubbles present. Flow was used to fill the cell with HCl or another electrolyte, but no flow was used during deposition unless specified. The liquid thickness was set by using a 250-nm-thick spacer layer between chips for Au and Cu; the liquid thickness therefore increases from about this value at the edge of the window to several micrometers in the center of the window due to window bulging. No spacer was used for Ni deposition; the minimum liquid thickness near the window edge was ~50 nm.

Electrochemical control was achieved through a two-terminal configuration consisting of a WE and a counter/reference electrode (C/RE). Both galvanostatic and potentiostatic conditions were used, with current or potential pulsed to examine growth kinetics and to minimize bubble generation. Irradiation of either the electrolyte or electrodes did not measurably alter the overall electrochemical characteristics during these experiments, consistent with other electrochemical liquid cell TEM experience (39, 40). Although the rapid diffusion of metal ions [$D = 10^9$ nm$^2$/s for Au (41, 42)] promises rapid ion removal once the voltage is set to zero, we circulated fresh electrolyte (for example, 0.1 M HCl) for at least 5 min using a syringe pump before each growth or erase experiment as a precaution to ensure removal of metal ions and radiolysis species.

### Au nanocrystal growth
For Au deposition, the electrodes were parallel strips of 30-nm-thick polycrystalline Au each with a 90-μm-long × 20-μm-wide active area defined by a silicon dioxide passivation layer. The electrodes were separated by 20 μm, and the beam was placed between the two electrodes. Multiple depositions were carried out in each cell, using one electrode as the WE and changing between other electrodes for the C/RE, as the C/RE is etched during the experiments. We tested the result of liquid flow with direction from C/RE to WE, but we found no visible effect from flow rates of <20 μl/min.

## Cu nanocrystal growth

For Cu deposition, the three electrodes each had a different active area. The electrode used as the WE was 5 μm wide and that used as the C/RE was 20 μm wide, with a 5-μm gap between electrodes. The active areas were 10 and 40 μm$^2$, respectively.

## Ni nanocrystal growth

For Ni deposition, two electrodes were arranged in a comb configuration separated by a 5-μm gap. One electrode had nine fingers, each 5 μm wide, with a total exposed area of 900 μm$^2$ and the second had nine fingers, each 10 μm wide, with a total exposed area of 1800 μm$^2$. Either of these could be used as the WE. The C/RE was a large pad, 180 μm wide, with a total exposed area of 3600 μm$^2$ located 50 μm away from the edge of the comb electrode.

## Image analysis

Images were obtained in bright-field mode and recorded at 30 frames/s at a region within the viewing window of the liquid cell. To stimulate and record the process of nanocrystal growth, as in Fig. 1, the beam diameter was fixed at several micrometers to irradiate a cylinder of liquid. After growth, the beam was spread as in Fig. 3 and figs. S3 and S4 to show the entire deposited region and the surroundings.

## SUPPLEMENTARY MATERIALS

Supplementary material for this article is available at http://advances.sciencemag.org/cgi/content/full/3/7/e1700234/DC1

movie S1. Formation of Au nanocrystals in 0.1 M HCl under a pulsed current of −60 nA for 10 s, followed by 0 nA for 10 s.

movie S2. Dissolution of the Au CE in 0.1 M HCl under linear potential sweeping.

movie S3. Formation of Au nanocrystals in 0.1 M HCl during step potential shown in fig. S2A.

movie S4. Electrochemical deposition at the Au CE in 0.1 M HCl during alternating square wave potential shown in fig. S2B.

movie S5. Formation of Au nanocrystals in 0.1 M HCl under a pulsed current of −60 nA for 5s, followed by 0 nA for 5 s.

movie S6. Oxidative etching of Au nanocrystals in 0.1 M HCl under electron beam irradiation at a dose rate of 260 $e^-$/Å$^2$·s.

movie S7. Formation of Cu nanocrystals in 0.1 M HCl during linear potential sweeping.

movie S8. Formation of Ni nanocrystals in 0.1 M HCl during linear potential sweeping.

fig. S1. Complete set of images and electrical data for the deposition experiment shown in Fig. 1 and movie S1.

fig. S2. Potential control of deposition.

fig. S3. Sequential bright-field TEM images of writing and erasing Au nanocrystals.

fig. S4. Relationship between pulse width and deposition morphology and quantity.

fig. S5. Concentration and diffusion profile of Au ions in the electrochemical + radiolytic deposition process of Au nanocrystals.

fig. S6. Images showing writing and erasing of Au from movies S5 and S6.

fig. S7. Electrochemical data for deposition of Cu and Ni nanocrystals.

fig. S8. Overall process of metal nanocrystal growth via ion release under electrochemical control and subsequent reduction to form nanocrystals under radiolytic control.

table S1. The activation potential for electrochemical growth of metal nanocrystals in 0.1 M HCl. References (43–47)

## REFERENCES AND NOTES

1. I. Utke, S. Moshkalev, P. Russell, Eds., *Nanofabrication Using Focused Ion and Electron Beams - Principles and Applications* (Oxford Univ. Press, 2012).
2. Y. Xia, Y. Xiong, B. Lim, S. E. Skrabalak, Shape-controlled synthesis of metal nanocrystals: Simple chemistry meets complex physics? *Angew. Chem. Int. Ed.* **48**, 60–103 (2009).
3. D. Mijatovic, J. C. T. Eijkel, A. van den Berg, Technologies for nanofluidic systems: Top-down vs. bottom-up—A review. *Lab Chip* **5**, 492–500 (2005).
4. C. Vieu, F. Carcenac, A. Pépin, Y. Chen, M. Mejias, A. Lebib, L. Manin-Ferlazzo, L. Couraud, H. Launois, Electron beam lithography: Resolution limits and applications. *Appl. Surf. Sci.* **164**, 111–117 (2000).
5. C.-S. Kim, S.-H. Ahn, D.-Y. Jang, Review: Developments in micro/nanoscale fabrication by focused ion beams. *Vacuum* **86**, 1014–1035 (2012).
6. W. F. van Dorp, C. W. Hagen, A critical literature review of focused electron beam induced deposition. *J. Appl. Phys.* **104**, 081301 (2008).
7. R. D. Piner, J. Zhu, F. Xu, S. Hong, C. A. Mirkin, "Dip-pen" nanolithography. *Science* **283**, 661–663 (1999).
8. H. Zheng, Y. S. Meng, Y. Zhu, Frontiers of in situ electron microscopy. *MRS Bull.* **40**, 12–18 (2015).
9. M. Bresin, A. Chamberlain, E. U. Donev, C. B. Samantaray, G. S. Schardien, J. T. Hastings, Electron-beam-induced deposition of bimetallic nanostructures from bulk liquids. *Angew. Chem. Int. Ed.* **52**, 8004–8007 (2013).
10. M. Huth, F. Porrati, C. Schwalb, M. Winhold, R. Sachser, M. Dukic, J. Adams, G. Fantner, Focused electron beam induced deposition: A perspective. *Beilstein J. Nanotechnol.* **3**, 597–619 (2012).
11. J. F. Friedman, T. M. Miller, J. K. Friedman-Schaffer, A. A. Viggiano, G. K. Rekha, A. E. Stevens, Electron attachment to Ni(PF$_3$)$_4$ and Pt(PF$_3$)$_4$. *J. Chem. Phys.* **128**, 104303–104306 (2008).
12. S. Engmann, M. Stano, Š. Matejčík, O. Ingólfsson, The role of dissociative electron attachment in focused electron beam induced processing: A case study on cobalt tricarbonyl nitrosyl. *Angew. Chem. Int. Ed.* **50**, 9475–9477 (2011).
13. R. J. Von Gutfeld, L. T. Romankiw, R. E. Acosta, Laser-enhanced plating and etching: Mechanisms and applications. *IBM J. Res. Dev.* **26**, 136–144 (1982).
14. M. den Heijer, I. Shao, A. Radisic, M. C. Reuter, F. M. Ross, Patterned electrochemical deposition of copper using an electron beam. *APL Mater.* **2**, 022101 (2014).
15. M. S. Chandrasekar, M. Pushpavanam, Pulse and pulse reverse plating—Conceptual, advantages and applications. *Electrochim. Acta* **53**, 3313–3322 (2008).
16. T. J. Woehl, K. L. Jungjohann, J. E. Evans, I. Arslan, W. D. Ristenpart, N. D. Browning, Experimental procedures to mitigate electron beam induced artifacts during in situ fluid imaging of nanomaterials. *Ultramicroscopy* **127**, 53–63 (2013).
17. Y. Liu, S. J. Dillon, Environmental electron microscopy: Electron beam effects in electrochemistry. *Microsc. Microanal.* **20**, 1616–1617 (2014).
18. C. G. Khoury, T. Vo-Dinh, Gold nanostars for surface-enhanced Raman scattering: Synthesis, characterization and optimization. *J. Phys. Chem. C Nanomater. Interfaces* **112**, 18849–18859 (2008).
19. C. A. Young, J. J. Kellar, M. L. Free, J. Drelich, R. P. King, Eds., *Innovations in Natural Resource Processing: Proceedings of the Jan. D. Miller Symposium*, Section 3: Hydrometallurgy (Society for Mining, Metallurgy, and Exploration Inc., 2005).
20. S. Cherevko, A. R. Zeradjanin, G. P. Keeley, K. J. J. Mayrhofer, A comparative study on gold and platinum dissolution in acidic and alkaline media. *J. Electrochem. Soc.* **161**, H822–H830 (2014).
21. S. Cherevko, A. A. Topalov, A. R. Zeradjanin, I. Katsounaros, K. J. J. Mayrhofer, Gold dissolution: Towards understanding of noble metal corrosion. *RSC Adv.* **3**, 16516–16527 (2013).
22. T. J. Woehl, J. E. Evans, I. Arslan, W. D. Ristenpart, N. D. Browning, Direct in situ determination of the mechanisms controlling nanoparticle nucleation and growth. *ACS Nano* **6**, 8599–8610 (2012).
23. J. H. Park, N. M. Schneider, J. M. Grogan, M. C. Reuter, H. H. Bau, S. Kodambaka, F. M. Ross, Control of electron beam-induced Au nanoparticle growth kinetics through solution chemistry. *Nano Lett.* **15**, 5314–5320 (2015).
24. J. M. Grogan, N. M. Schneider, F. M. Ross, H. H. Bau, Bubble and pattern formation in liquid induced by an electron beam. *Nano Lett.* **14**, 359–364 (2014).
25. N. M. Schneider, M. M. Norton, B. J. Mendel, J. M. Grogan, F. M. Ross, H. H. Bau, Electron–water interactions and implications for liquid cell electron microscopy. *J. Phys. Chem. C* **118**, 22373–22382 (2014).
26. H.-G. Liao, K. Niu, H. Zheng, Observation of growth of metal nanoparticles. *Chem. Commun.* **49**, 11720–11727 (2013).
27. K. L. Jungjohann, S. Bliznakov, P. W. Sutter, E. A. Stach, E. A. Sutter, In situ liquid cell electron microscopy of the solution growth of Au–Pd core–shell nanostructures. *Nano Lett.* **13**, 2964–2970 (2013).
28. J. Wu, W. Gao, J. Wen, D. J. Miller, P. Lu, J.-M. Zuo, H. Yang, Growth of Au on Pt icosahedral nanoparticles revealed by low-dose in situ TEM. *Nano Lett.* **15**, 2711–2715 (2015).
29. Y. Jiang, G. Zhu, F. Lin, H. Zhang, C. Jin, J. Yuan, D. Yang, Z. Zhang, In situ study of oxidative etching of palladium nanoparticles by liquid cell electron microscopy. *Nano Lett.* **14**, 3761–3765 (2014).
30. S. Jesse, A. Y. Borisevich, J. D. Fowlkes, A. R. Lupini, P. D. Rack, R. R. Unocic, B. G. Sumpter, S. V. Kalinin, A. Belianinov, O. S. Ovchinnikova, Directing matter: Towards atomic scale 3D nanofabrication. *ACS Nano* **10**, 5600–5618 (2016).
31. E. U. Donev, J. T. Hastings, Electron-beam-induced deposition of platinum from a liquid precursor. *Nano Lett.* **9**, 2715–2718 (2009).
32. R. R. Unocic, A. R. Lupini, A. Y. Borisevich, D. A. Cullen, S. V. Kalinin, S. Jesse, Direct-write liquid phase transformations with a scanning transmission electron microscope. *Nanoscale* **8**, 15581–15588 (2016).
33. I. Utke, P. Hoffmann, J. Melngailis, Gas-assisted focused electron beam and ion beam processing and fabrication. *J. Vac. Sci. Technol. B* **26**, 1197–1276 (2008).
34. W. F. van Dorp, C. W. Hagen, P. A. Crozier, P. Kruit, Growth behavior near the ultimate resolution of nanometer-scale focused electron beam-induced deposition. *Nanotechnology* **19**, 225305 (2008).

35. H.-G. Liao, H. Zheng, Liquid cell transmission electron microscopy study of platinum iron nanocrystal growth and shape evolution. *J. Am. Chem. Soc.* **135**, 5038–5043 (2013).

36. H.-G. Liao, D. Zherebetskyy, H. Xin, C. Czarnik, P. Ercius, H. Elmlund, M. Pan, L.-W. Wang, H. Zheng, Facet development during platinum nanocube growth. *Science* **345**, 916–919 (2014).

37. E. Atinault, V. De Waele, U. Schmidhammer, M. Fattahi, M. Mostafavi, Scavenging of $e_s^-$ and OH˙ radicals in concentrated HCl and NaCl aqueous solutions. *Chem. Phys. Lett.* **460**, 461–465 (2008).

38. Y. Furuya, T. Mashio, A. Ohma, M. Tian, F. Kaveh, D. Beauchemin, G. Jerkiewicz, Influence of electrolyte composition and pH on platinum electrochemical and/or chemical dissolution in aqueous acidic media. *ACS Catal.* **5**, 2605–2614 (2015).

39. M. J. Williamson, R. M. Tromp, P. M. Vereecken, R. Hull, F. M. Ross, Dynamic microscopy of nanoscale cluster growth at the solid–liquid interface. *Nat. Mater.* **2**, 532–536 (2003).

40. M. E. Holtz, Y. Yu, D. Gunceler, J. Gao, R. Sundararaman, K. A. Schwarz, T. A. Arias, H. D. Abruña, D. A. Muller, Nanoscale imaging of lithium ion distribution during in situ operation of battery electrode and electrolyte. *Nano Lett.* **14**, 1453–1459 (2014).

41. N. A. Bonner, E. H. Willes, Tracer diffusion and electric mobility of ions in aqueous solutions: A method for estimating the average charge of complex ions. *J. Chem. Eng. Data* **45**, 324–330 (2000).

42. M. Harada, K. Okamoto, M. Terazima, Diffusion of gold ions and gold particles during photoreduction processes probed by the transient grating method. *J. Colloid Interface Sci.* **332**, 373–381 (2009).

43. G. Alarnes-Varela, A. Costa-García, Determination of gold by anodic stripping voltammetry with carbon fiber ultramicroelectrodes. *Electroanalysis* **9**, 1262–1266 (1997).

44. N. Meepun, S. Siriket, S. Dejmanee, R. Ratana-Ohpas, Stripping chronopotentiometry: An alternative method for the determination of gold in geological samples. *Walailak J. Sci. Technol.* **7**, 61–67 (2010).

45. D. Jagner, Potentiometric stripping analysis. *Analyst* **107**, 593–599 (1982).

46. J. Opydo, Cathodic adsorptive stripping voltammetry for estimation of the forest area pollution with nickel and cobalt. *Microchim. Acta* **137**, 157–162 (2001).

47. M. M. Nicholson, Anodic stripping voltammetry of nickel at solid electrodes. *Anal. Chem.* **32**, 1058–1062 (1960).

**Citation:** J. H. Park, D. A. Steingart, S. Kodambaka, F. M. Ross, Electrochemical electron beam lithography: Write, read, and erase metallic nanocrystals on demand. *Sci. Adv.* **3**, e1700234 (2017).

# ScienceAdvances

## Electrochemical electron beam lithography: Write, read, and erase metallic nanocrystals on demand

Jeung Hun Park, Daniel A. Steingart, Suneel Kodambaka and Frances M. Ross

| | |
|---|---|
| **ARTICLE TOOLS** | http://advances.sciencemag.org/content/3/7/e1700234 |
| **SUPPLEMENTARY MATERIALS** | http://advances.sciencemag.org/content/suppl/2017/07/10/3.7.e1700234.DC1 |
| **PERMISSIONS** | http://www.sciencemag.org/help/reprints-and-permissions |

Use of this article is subject to the Terms of Service